

Supplementary Information

Kinetic Monte Carlo applied to the electrochemical study of the Li-ion/graphite system

E.M. Gavilán-Arriazu^{1,2}, O.A. Pinto², B.A. López de Mishima², D.E. Barraco³, O.A. Oviedo¹,
E.P.M Leiva^{1,*}

¹Departamento de Química Teórica y Computacional, Facultad de Ciencias Químicas, Universidad Nacional de Córdoba, INFIQC, Córdoba, Argentina.

²Instituto de Bionanotecnología del NOA (INBIONATEC). Universidad Nacional de Santiago del Estero (UNSE); CONICET. RN 9, Km 1125. G4206XCP, Santiago del Estero, Argentina.

³Facultad de Matemática, Astronomía y Física, IFEG-CONICET, Universidad Nacional de Córdoba, Córdoba, Argentina

maxigavilan@hotmail.com, eze_leiva@yahoo.com.ar

S.1. Nomenclature

M Total number of lattice sites that can be occupied by Li ions

N_x, N_y, N_z Number of lattice sites in the x, y and z directions

L_x, L_y, L_z Lateral dimensions of the simulation box along the x, y and z axis

ε Lennard-Jones potential depth

r_m Lennard-Jones characteristic distance

κ Parameter controlling the strength of Li-Li repulsive interactions

α Exponent controlling the range of Li-Li repulsive interactions

r_b Scaling distance

μ Chemical potential

γ Occupational energy

r Distance between two Li-ions

N_{op} Number of nearest neighbor sites in different graphite layers

N_{ip} Number of nearest neighbor sites in the same graphite layer
 c_j Occupational term for lattice site j
 Γ Reaction rate
 ν_0 Preexponential factor
 H^*, H_I, H_F Hamiltonian for activated, initial and final states respectively
 k_B Boltzmann constant
 T Temperature
 Δ^*_σ Energy barrier for event σ
 α_{BV} Symmetry factor for charge transfer
 x Fraction of graphite lattice sites occupied by Li-ions
 ν_{sr} Potential sweep rate
 E Electrode potential vs Li / Li^+
 E_0, E_f Initial and final potential for the simulation of cyclic voltammograms
 E_{pr}, E_{po} Voltammetric peak potential for reductive and oxidative processes.
 i_{pr}, i_{po} Values of voltammetric reduction and oxidation current peaks
 Λ Dimensionless kinetic factor (same as defined in reference [1])
 $R_{diff}, R_\Omega, R_{ct}$ Diffusion, ohmic and charge transfer resistances
 D, D_x, D_y Diffusion coefficient, and diffusion coefficient in the x and y directions
 d_s Distance parameter
 $area_s$ Area of the surface that separates two neighboring unit cells
 I_{Cott} Cottrell current
 $\tau_{y,d}$ Diffusion time constant
 ΔQ Total charge inserted after a potential step
 D_{Li} Chemical diffusion coefficient
 D_j Jump diffusion coefficient
 Θ Thermodynamic factor

λ Characteristic jump distance

d System dimension

i_0 Exchange current

j_0 Exchange current density

A_{xz} Cross-sectional area of the electrode surface in contact with the electrolyte

Q Charge corresponding the full Li-ion occupation of the system

k_1, k_{-1} Forward and reverse rate constants

F Faraday constant

R Gas constant

g Frumkin-type isotherm interaction parameter

c_{Li^+} Lithium-ion concentration in bulk solution

GCMC Grand Canonical Monte Carlo

GC-kMC Grand Canonical kinetic Monte Carlo

C-kMC Canonical kinetic Monte Carlo

S.2. Theoretical model

S.2.1. Graphite lattice-gas

A lattice-gas model was used to emulate the insertion of Lithium ions in a graphite particle. The lattice was constructed as follows: each lattice site is located at the center of carbon hexagons and at the half distance between two graphene layers with AA stacking. According to the graphite unit cell constants, the distance between adjacent lattice planes is 3.35 Å and the distance to the first nearest neighbors in the same plane is 2.46 Å.

The lattice used in this work consists in a total of $M = N_x \times N_y \times N_z$ intercalation sites in graphite, where N_x , N_y and N_z are the number of lateral sites along the X, Y and Z axes.

The Z-direction is considered to be perpendicular to the surface, while the X-Y plane is parallel to the lattice-gas layers, thus N_z determines the number of bidimensional $N_x \times N_y$ lattice planes. L_x , L_y and L_z are the corresponding axis lengths.

S.2.2. Events allowed in the different types of simulations

Grand Canonical Monte Carlo Simulations (GCMC)

The events allowed in GCMC were insertion/deletion of Li ions into/from the lattice sites (event I, Figure S1a). The probability of the occurrence of these events was evaluated using the GCMC standard procedure. Periodic boundary conditions (PBC) were applied in all directions, except those explicitly indicated.

Kinetic Monte Carlo Simulations (kMC)

Regarding kMC simulations, diffusion, insertion and deletion events were considered (Figure S1b); but at difference with GCMC, in the kinetic model the following conditions were imposed:

- Li ions can only be exchanged (intercalated or deintercalated) with the environment on the left hand side of the simulation box, event (II) in Figure S1b. These events were only allowed in GC-kMC simulations.
- Li ions can only jump to first neighboring lattice sites in the same layer, event (III) in Figure S1b.
- No jumps are allowed in the Z direction, restriction (IV) in Figure S1b, since the activation energy for this type of events is very high [2].
- In the case of GC-kMC, Li diffusional motion is restricted to the length of the simulation box along the y axis, L_y , see restriction (V) in Figure S1b. This restriction is removed for Canonical kinetic (C-kMC) runs, used to evaluate diffusion coefficients. Diffusion was in all cases free along the X axis, where periodic boundary conditions are imposed.
- PBC are also imposed in the Z direction for the calculation of all interactions.

In summary, in the present kinetic simulations, some cases were considered where ion exchange with the solution was allowed (denoted with GC-kMC) and other cases where the number ions was kept constant denoted with (C-kMC).

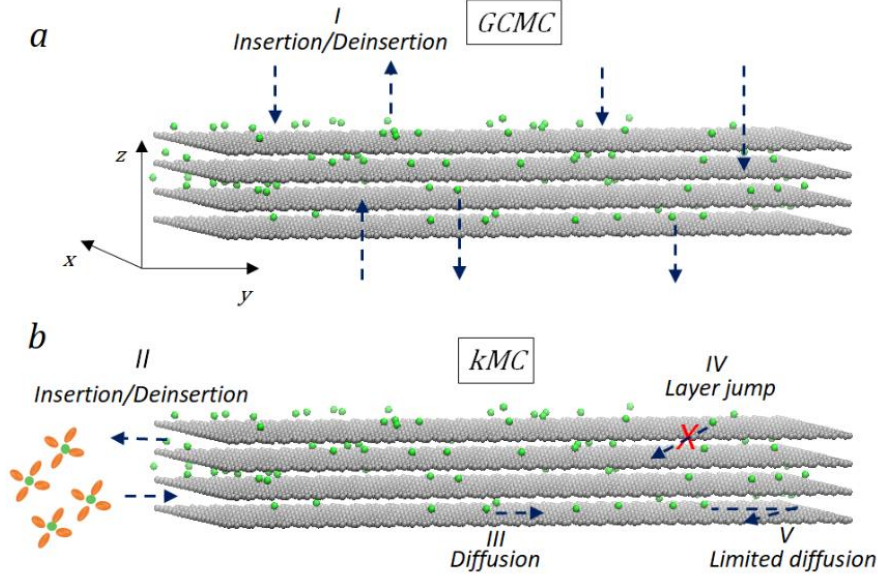


Figure S1: Scheme of events allowed and restrictions set for the different types of simulations used in this work. Top: Grand Canonical Monte Carlo simulations. Bottom: kinetic Monte Carlo simulations. The processes and restrictions correspond to: (I) Ion exchange with a reservoir at a constant chemical potential μ (II) Ion exchange with a solution located on the left of the figure, regulated by a potential difference E , which is linearly related to μ . (III) Diffusion within the same layer. (IV) Diffusion between neighboring layers is prohibited. (V) Diffusion restricted by a hard wall on the right hand side of the simulation box. Lithium ions are represented as green spheres and graphite carbon atoms are in grey. The green spheres surrounded by orange balloons represent the electrolyte, and are only placed with illustrative purposes.

S.2.3. Arrhenius and Butler-Volmer equations

The rate equation used in the model simply consists of Arrhenius (S1) and Butler-Volmer approximation (S2) terms:

$$\Gamma = v_0 \exp\left(-\frac{H^* - H_I}{k_B T}\right) \quad (\text{S1})$$

$$H^* = \Delta_{\sigma}^* + \alpha_{BV} (H_I + H_F) \quad (\text{S2})$$

where ν_0 is a pre-exponential factor, H^* is the Hamiltonian for the activated state, H_I and H_F are the Hamiltonians for the initial and final state respectively, k_B is Boltzmann constant and T the absolute temperature. Unless otherwise stated, $T = 296\text{K}$. In equation (S2) Δ_σ^* is the energy barrier for event σ ($\sigma = \text{diff}$ for diffusion and $\sigma = i/d$ for a particle insertion or deletion) and α_{BV} the symmetry factor for charge transfer. The rate equation used in the present work is obtained replacing equation (S2) into equation (S1).

S.3. Cyclic voltammetry

S.3.1. Code adaptation

The cyclic voltammetry algorithm is introduced into kMC as follows:

- 1) A potential sweep rate, ν_{sr} , an initial potential value, E_0 , and a final potential E_f are chosen.
- 2) The potential increment at each time step is calculated according to $\Delta E_{i+1} = \nu_{sr} \Delta t_i$, where Δt_i is the time increment calculated within the usual kMC scheme at time t_i .
- 3) The potential is changed at each step according to $E_{i+1} = E_i + \Delta E_{i+1}$.
- 4) When the potential reaches the final value (E_f) the scan direction is reversed $E_{i+1} = E_f - \Delta E_{i+1}$.
- 5) The algorithm finishes when the potential reaches the initial value E_0 .

The present study considers cyclic voltammetry for small system sizes $N_x = 24$ ($L_x = 59.04 \text{ \AA}$), $N_y = 24$ ($L_y = 51.12 \text{ \AA}$), $N_z = 4$ ($L_z = 13.40 \text{ \AA}$), because the simulations are computationally very demanding.

S.3.2. Analysis of the dependence of the current and potential peak with potential sweep rate

Here, we analyze the relationship between peak current i_p and sweep rate v_{sr} , also employed in the literature to analyze the present electrochemical process.

The relationship between a voltammetric current peak and the potential sweep rate can be written as $i_p = av_{sr}^b$ [3], where a and b are adjustable values. b can thus be obtained from the slope of the linear relationship $\log i_p = \log a + b \log v_{sr}$. The limiting values of b are 0.5 for diffusion control and 1 for surface process control, while intermediate b values are expected for a mixed behavior [3]. log-log plots for the present simulated reduction and oxidation current peaks, as a function of the sweep rate for the $II \leftrightarrow I$ transition, are shown in Figure S2a.

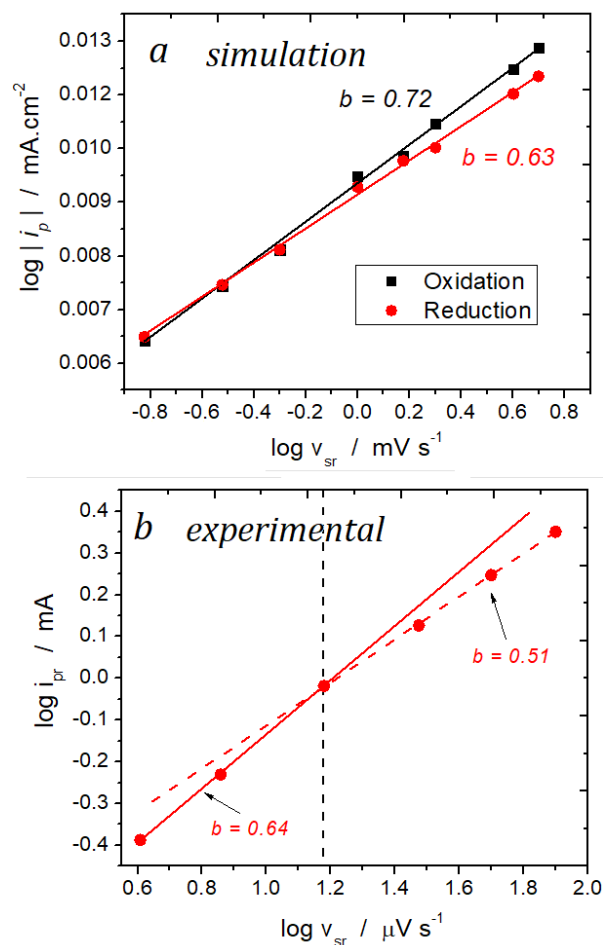


Figure S2: Log-log plots for the relationship between the voltammetric current peak (i_{pr2}, i_{po2}) and the potential sweep rate due to the Stage I-Stage II transition. a) Simulated results. Black squares (black linear fit) correspond to the oxidative scan. Red circles (red linear fit) correspond to the reductive scan. b) experimental data from ref [4] for the reductive

current peak due to the Stage I-Stage II transition. The red dashed line is the linear fit for the larger scan rates and solid red line is the linear fit for lower sweep rates. The vertical black dashed line separates both regimes.

Linear fits of the logarithmic plots yield $b \approx 0.7$ for the oxidation and $b \approx 0.63$ for the reduction peaks. The same analysis for experimental data, taken from Levi et al. [4], exhibits two different dependences of i_p with v_{sr} , as shown in Figure S2b. For the largest sweep rates, the slope b is 0.51 (linear fit is shown as a dashed red line) and for the slowest sweep rates $b = 0.64$ (linear fit is shown as a solid red line). The vertical black dashed line indicates the separation of both regions. Data taken from Kulova et al data (Figure 6 of reference [5]) deliver similar results. In the case of the experimental data from Figure S2b, the slope change at slow sweep rates is only observed with thin graphite electrodes. For thick electrodes only one slope, $b \approx 0.5$, is found for all sweep rates [6].

It must be emphasized that the present simulations involve very thin electrodes (0.0051 μm). Thus, the changes in the voltammetric profiles with the sweep rate observed in the present work are due to kinetic limitations for the insertion (deletion) of ions into (out from) graphite and not by their diffusion inside graphite. The last process should be the limiting process for experimental graphite flakes, which are much thicker (of the order of μm).

The hysteresis can also be observed by analyzing $|E_{po2} - E_{pr2}|$ as a function of v_{sr} and $\log v_{sr}$. Figure S3 shows the potential difference $|E_{po2} - E_{pr2}|$ as a function of v_{sr} and $\log v_{sr}$ for the simulations (a and b) and experimental data from reference [4] (c and d). The experimental and simulated $|E_{po2} - E_{pr2}|$ vs v_{sr} plots are qualitatively similar (Figure S3a and S3c). The similarity becomes stronger when looking at $|E_{po2} - E_{pr2}|$ vs $\log v_{sr}$ representation (Figure S3b and S3d), where in both cases a linear relationship becomes evident.

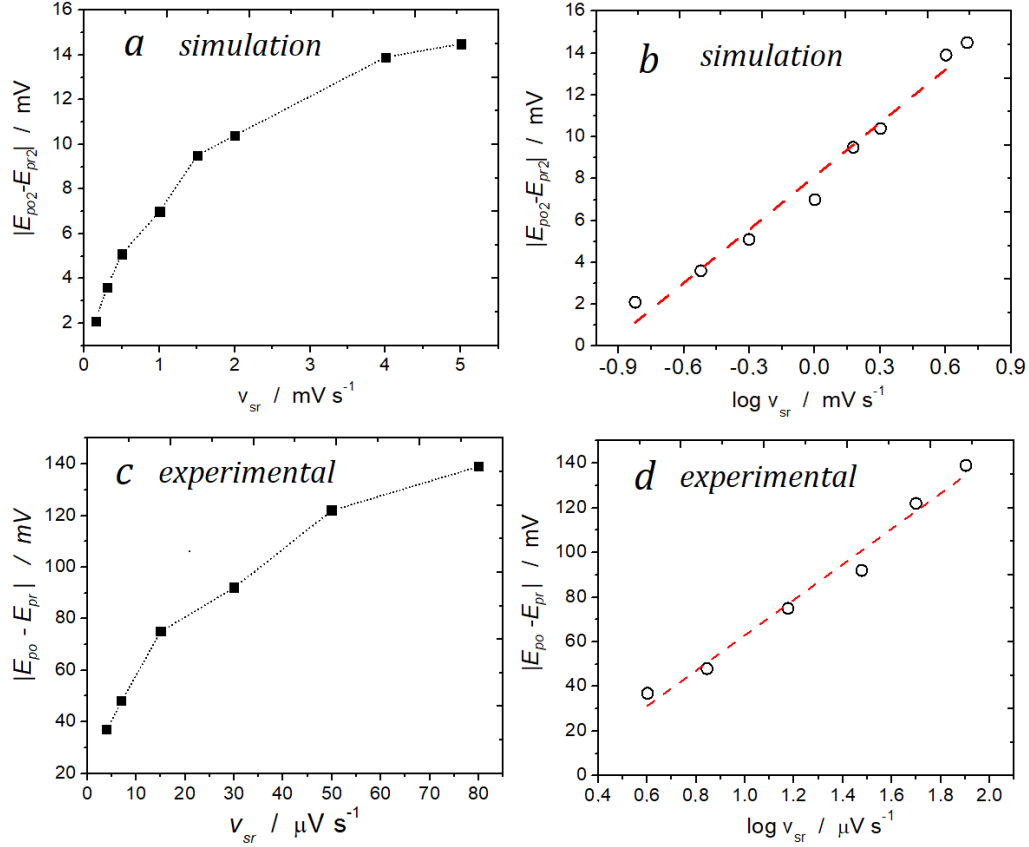


Figure S3: The difference between the anodic and the cathodic peaks for the Stage I-Stage II transition as a function of potential sweep rate. Upper plots: simulation. Lower plots: experimental data from ref. [4].

S.3.3. Simulated voltammograms for different graphite sizes

To analyze the effect of graphite size in the simulations, we have considered the behavior of the systems as a function of the lateral size (L_y) at a given sweep rate, $v_{sr} = 1.00 \text{ mV.s}^{-1}$. Variations of the number of layers (L_z) are not considered, since preliminary simulations showed that this parameter does not have a large effect as compared with L_y changes. This is expected, since particles are allowed to move in the X-Y plane but not in the Z direction.

The peaks separation ($|E_{po} - E_{pr}|$) and the peak half-width increase as the lateral size L_y increases (Figure S4). This is a expected behavior, since as L_y becomes smaller, the system

equilibrates more rapidly at a given sweep rate. These features are in qualitative agreement with the experimental results presented in Figure 2 of Levi et al [7], where these authors studied the voltammetric behavior of thick, thin and ultrathin electrodes.

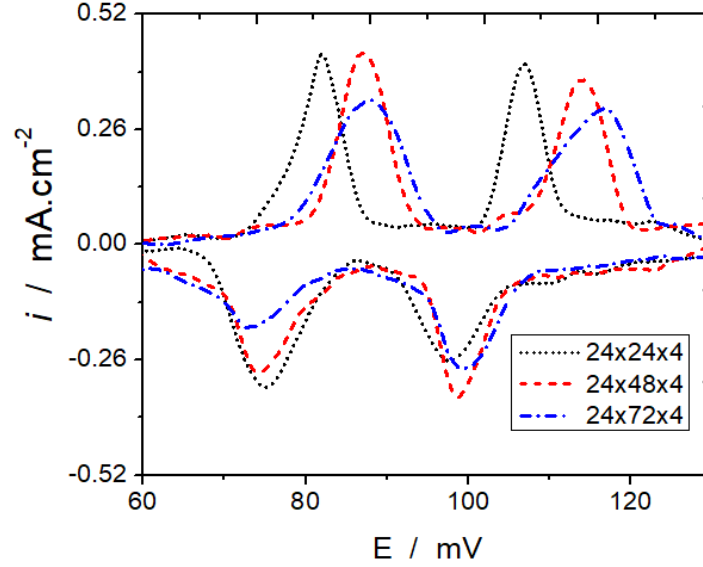


Figure S4: Voltammograms for three different L_y sizes. Sweep rate of 1 mV.s^{-1} .

S.4. Validation of the potentiostatic step kMC procedure in comparison with literature results assuming Langmuirian conditions.

Montella [1] has derived theoretical expressions for the response of ion-insertion electrodes to a potential step assuming linear diffusion, restricted diffusion conditions and possible limitations by insertion reaction kinetics. In this work is proposed that the response of the current versus time under potentiostatic conditions depends on a dimensionless kinetic factor Λ , which contains information on the diffusional, kinetic and ohmic characteristics of the system under consideration. This parameter is defined as:

$$\Lambda = \frac{R_{diff}}{R_{\Omega} + R_{ct}} \quad (3)$$

Where R_{diff} , R_{Ω} and R_{ct} are the diffusion, ohmic drop and charge transfer resistances, respectively, in Ω .

The simulations from the present study are based on a Hamiltonian containing the interactions between the particles of the system, so that both, the diffusional and kinetic parameters emerging from the model, exhibit a considerable complexity. The diffusion coefficient is not a constant and depends on the occupation of the system, so that a diffusion time constant cannot be straightforwardly defined as in Montella's work. However, it becomes mandatory to validate our model by comparing our results with the useful results of the simplified modeling, so that we must first reproduce some of the results obtained by Montella, adapting the present model to the conditions presented on his work [1]. This is strictly necessary since we are connecting a theoretical model with experimental results, using a Hamiltonian fitted with experimental data; thus, it seems obvious to start with the simplest approach and then change the conditions to simulate more complex conditions.

Model Adaptation

There are some restrictions that must be imposed to the present model to compare its predictions with the results of Montella's model:

- 1) The interaction between the inserted particles will be neglected.
- 2) For the simulations presented here with validation purposes, the only two phenomena allowed will be particle insertion and diffusion. Particle removal will not be allowed by setting a very extreme (negative) potential, but this phenomenon could be simulated straightforwardly.
- 3) Particle insertion is allowed at the left side of the simulation box ($y = 0$), while the other side is closed and restricts particle diffusion ($y = L_y$).
- 4) The simulations will not consider ohmic drop resistance, so $R_\Omega = 0$.

For these comparative studies $N_x = N_y = N$ and $N_z = 1$, so $M = N^2$.

Δ derivation for the lattice model, assuming Langmuirian conditions.

The insertion of an ion A^+ into graphite is described by the follow reaction:



Where $*$ denotes the insertion site, e^- an electron neutralizing the inserted ion and $(A^+, e^-)^*$ the intercalated species. Following the reactions stated by Montella [1], the Li-ion insertion rate ν in units of moles per unit area and unit time for this reaction is:

$$\nu = K_r c_M [c_{\max} - c(0, t)] - K_o c(0, t) \quad (S5)$$

where $c(0, t)$ is the ion concentration at the interphase, c_{\max} is the saturation concentration of the graphite lattice, K_r and K_o are reduction and oxidation rate constants, respectively, and c_M is bulk ion concentration. Let us connect now this definition with the present definition of reaction rate Γ .

Under Langmuirian conditions, the insertion/deinsertion rate Γ has an occupation-independent value at a fixed potential, since there is no interaction between particles:

$$\Gamma = \nu_0 \exp\left(-\frac{\Delta_{\sigma}^*}{k_B T}\right) \exp\left(-\frac{(\gamma - \mu) \sum_i^N c_i^f - (\gamma - \mu) \sum_i^N c_i^0}{2k_B T}\right) \quad (S6)$$

Where c_i^f and c_i^0 are the occupational terms for the final and the initial states of a given site and $\Delta_{\sigma}^* = \Delta_{i/d}^* = 0.655$ eV. Thus, for a Langmuirian insertion step, the insertion rate at a given site, say j is:

$$\Gamma_r = \nu_0 \exp\left(-\frac{\Delta_{\sigma}^*}{k_B T}\right) \exp\left(-\frac{(\gamma - \mu)(c_j^f - c_j^0)}{2k_B T}\right) = \nu_0 \exp\left(-\frac{\Delta_{\sigma}^*}{k_B T}\right) \exp\left(-\frac{(\gamma - \mu)}{2k_B T}\right) \quad (S7)$$

While the deinsertion rate from site j is given by:

$$\Gamma_o = \nu_0 \exp\left(-\frac{\Delta_{\sigma}^*}{k_B T}\right) \exp\left(-\frac{(\gamma - \mu)(c_j^f - c_j^0)}{2k_B T}\right) = \nu_0 \exp\left(-\frac{\Delta_{\sigma}^*}{k_B T}\right) \exp\left(\frac{(\gamma - \mu)}{2k_B T}\right) \quad (S8)$$

It only remains to connect the rates Γ_r and Γ_o given in units of $\frac{1}{\text{time site}}$ with the rates

$K_r c_M$ and K_o presented in equation (S5), which are given in units of $\frac{\text{moles}}{\text{time surface concentration}}$. To set this equivalence, we note that:

$$\frac{\text{moles}}{\text{time surface concentration}} = \frac{\text{moles}}{\text{time surface} \frac{\text{moles}}{\text{volume}}} = \frac{\text{volume}}{\text{time surface}}$$

If we now denote with d_s the (volume/surface) ratio of the unit cell where a Li ion is inserted, we have the equivalences:

$$K_r c_M = \Gamma_r d_s \quad (\text{S9})$$

$$K_o = \Gamma_o d_s \quad (\text{S10})$$

So that replacing (S9) and (S10) into equation (S5) we get:

$$v = \Gamma_r d_s [c_{mas} - c(0, t)] - \Gamma_o d_s c(0, t) \quad (\text{S11})$$

According to the definition given in Montella's article [1], we have

$$\Lambda = \frac{|v_c| L_y / D}{1 + R_\Omega F A |v_E|} \quad (\text{S12})$$

Where v_c is $(\delta v / \delta c)_E$ and v_E is $(\delta v / \delta E)_c$. For the present simulations, $R_\Omega = 0$, so that

$$\Lambda = \frac{|v_c|}{D / L_y} \quad (\text{S13})$$

Thus, derivation of equation (S8) with respect to the interphase concentration yields v_c :

$$v_c = -\Gamma_r d_s - \Gamma_o d_s \quad (\text{S14})$$

and upon replacement in (S13):

$$\Lambda = \frac{|\Gamma_r d_s - \Gamma_o d_s|}{D / L_y} \quad (S15)$$

In the case of a large oxidation (deinsertion) barrier or extreme reduction potential conditions $\Gamma_o d_s$ becomes negligible, then;

$$\Lambda = \frac{|\Gamma_r d_s|}{D / L_y} \quad (S16)$$

Since the inserted particles are non-interacting, D does not change with ion concentration and $D = D_{y,0}$. Replacing in equation (S16):

$$\Lambda = \frac{|\Gamma_r d_s|}{D_{y,0} / L_y} \quad (S17)$$

This equation states Λ in terms of the rates of charge transfer and diffusion. Γ_r is the reduction (i.e., insertion) rate in s^{-1} , $D = D_x = D_y$ is the diffusion coefficient along the Y-axis in the limit of very low occupations. $D_{y,x \rightarrow 0} = D_0 = 1 \times 10^{-8.34} \text{ cm}^2 \text{ s}^{-1}$. $N = 72$, so $L_y = 153.36 \text{ \AA}$ is the box length along the Y-axis. d_s is a distance parameter defined by a unit cell of a graphite layer containing a single C atom:

$$d_s = \frac{vol_s}{area_s} \quad (S18)$$

where vol_s is the volume hosting a single site and $area_s$ is the area of the surface that separates two adjacent unit cells. The origin of these quantities is illustrated in Figure S5, where Figure S5a shows the dimensions of the rectangle used to calculate $area_s$ and Figure S5b shows the box used to calculate vol_s . Using this figure, we get $vol_s = 17.55 \times 10^{-24} \text{ cm}^3 \cdot \text{site}^{-1}$ and $area_s = 8.22 \times 10^{-16} \text{ cm}^2 \text{ site}^{-1}$, so that $d_s = 2.13 \times 10^{-8} \text{ cm}$.

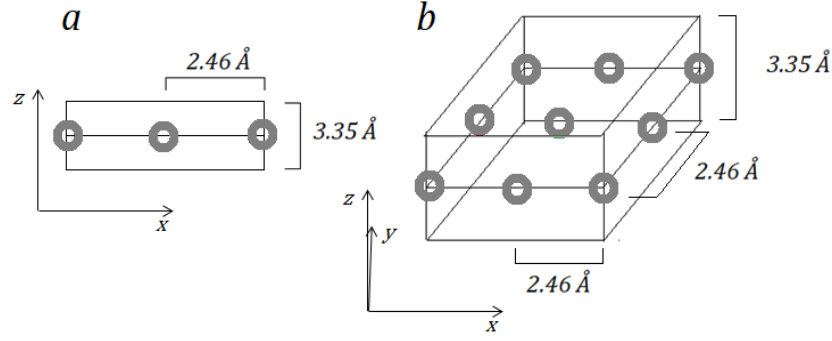


Figure S5: Schematic representations of the unit cells for the area at the interphasial region (a), and in the bulk of graphite (b). Grey circles represent intercalation sites.

According to the previous discussion, the free parameter determining Λ in equation (S17) is Γ_r , which is given by $\Gamma_r = v_0 \exp\left(-\frac{\Delta_r^*}{k_B T}\right) \exp\left[-\frac{(\gamma - \mu)}{2k_B T}\right]$. Consequently, by changing the insertion energy barrier Δ_r^* , different Λ values were obtained, as reported in Table S1.

Table S1: kinetic parameter Λ calculated with different energy barriers values Δ_r^* .

$\Delta_r^* [\text{eV}]$	Λ
0.300	145
0.375	8.0
0.400	2.88
0.425	1.1
0.450	0.41
0.475	0.15
0.500	0.06

The comparison will be made here with the results presented in figures 7a and 7b of reference [1], which shows results for the dimensionless form of the current as a function of time and its logarithm. With this purpose, it is necessary to calculate the Cottrell current (I_{Cott}), equation (S19), and the diffusion time constant ($\tau_{y,d}$), equation (S20), from:

$$I_{Cott} = \frac{\Delta Q}{\sqrt{\pi t \tau_{y,d}}} \quad (S19)$$

$$\tau_{y,d} = \frac{L^2}{D_{y,0}} \quad (S20)$$

and the current scaling factor $\frac{2\Delta Q}{\tau_{y,d}}$, where ΔQ is the total charge inserted after the potential step.

Figure S6 a and b show the results of the present kMC simulations for different values of Λ .

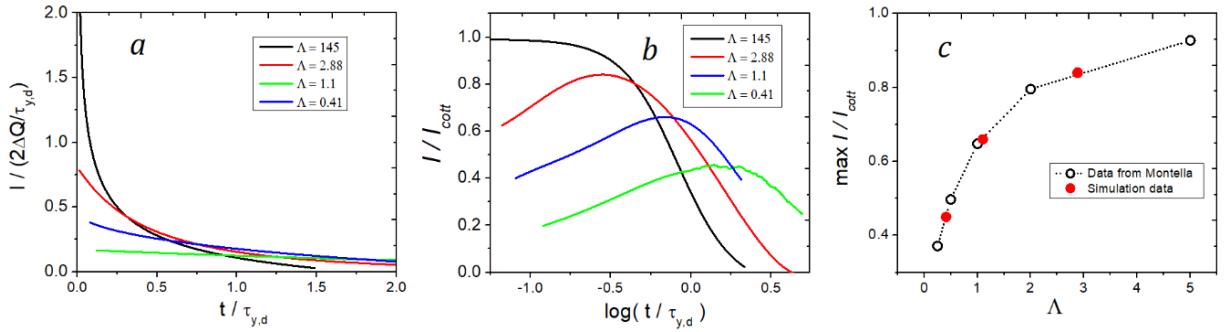


Figure S6: Results from kMC simulations for different Λ values, equation (S17) as indicated in the figure, according to the simplifications described in the text. a) Current vs time profiles b) Ratio of the Faradaic current to the limiting Cottrell equation (S19) plotted versus the decimal logarithm of time. c) Current peak maxima of the ratio of the Faradaic current to the limiting Cottrell equation (S19), as a function of the parameter Λ , (Eq. S17). The figure compares results from the present kMC simulations within the simplified model described in the text (red) with the data from Fig. 7a from Montella's work [1] (black).

It can be appreciated that the behavior of the system closely follows that obtained by Montella's theoretical work (see Figure 7a and b of [1]). As ion transfer kinetics at the interphase becomes slower as compared with ion diffusion (small Λ), a maximum becomes evident in the $I(t)$ vs $\log(t)$ curves. This maximum shifts to longer times for decreasing Λ values. To illustrate the agreement between the present simulations and Montella's results, Figure S6c shows a plot with the normalized current at the maximum as function of Λ . The simulated results are in red, while the calculated data from ref [1] are in black (Figure S6c). An excellent agreement is evident.

After showing that the present simulations can mimic the potentiostatic behavior described assuming Langmuirian conditions, a step forward may be taken, assuming more realistic interaction energies.

From equation (S17) it is clear that, if the charge transfer resistance is a function of occupation, then Λ should change with time. Furthermore, as the diffusion coefficient D also depends on occupation, it should also change with time as charge is inserted in or taken away from the system. This has concomitant changes in R_{diff} and in Λ too. The previous argument shows that the description of the current profiles in terms of the changes of Λ turns the analysis rather complex.

S.5. Discussion regarding Cyclic Voltammetry and Chronoamperometry

The present potentiodynamic (Section 3.1) and chronoamperometric (Section 3.2) simulations, as well as the experimental counterpart from the literature, indicate different roles of phase coexistence in intercalation and deintercalation processes. This is consistent with the analysis that can be made from the frames of the simulations. This is concluded by connecting the electrochemical responses in i , x and $it^{1/2}$ with the corresponding configurational arrangements that are obtained along the simulations. In this way, the minimum found between peaks p_1 and p_2 in the $it^{1/2}$ vs $\log t$ representations can be linked to the phenomenon of stage coexistence close to the interphase, found at the beginning of the chronoamperometric step. This phenomenon is particularly relevant when passing from a potential where a pure stage is established at the steady state (for example, stage II at E_3) to a potential where other stage can be formed (E_4 or E_5). The question now arises: Why is p_1 predominant in intercalation, while p_2 prevails in deintercalation? To answer this, we compare the height of p_1 at $E_3 \rightarrow E_5$ (Figure 4c) with the corresponding height in $E_3 \rightarrow E_4$ (Figure 4f). While p_2 is in the same order of magnitude in both cases, the height of p_1 is strongly changing in both situations, being considerably larger for the bigger potential step, as mentioned before. Let us focus on p_1 , then. The changes in p_1 can be understood if we think that, when the system jumps abruptly to a very negative insertion

potential, ion insertion rate is faster as compared with that of a small potential step from the same initial potential, while the diffusion rates remain the same. Since the minimum is related to stage coexistence, the height of p_1 can be associated with the phenomenon occurring immediately before, i.e. Li ion insertion. If the particles were non-interacting, Li-ions would rapidly spread to the inner part of the electrode. However, since the interaction between lithium ions in the same layer is attractive, Li ions accumulate at the interphase while being inserted. We must acknowledge that several of the present conclusions have been put forward by Levi at [8]. However, these assessments are now supported by an atomistic picture.

Contrary to the observation made at intercalation, in deintercalation p_2 is bigger than p_1 for the $E_5 \rightarrow E_3$ potential step and only one peak remains at the step $E_4 \rightarrow E_3$. Comparing the height and position of the peaks in both potential steps it is found that the peak for $E_4 \rightarrow E_3$ (Figure 6f) coincides with p_2 at $E_5 \rightarrow E_3$ (Figure 6c). The behavior of the p_2 component is here similar to that observed in the intercalation case, where p_2 had a similar magnitude for both potential steps. This similar behavior of p_2 for intercalation and deintercalation suggests that the peak in Figure 6f is due to the p_2 process, while p_1 has disappeared.

At this point we can connect the simulations with experimental results. As commented in the introduction section, Levi et al [8,9] observed two peaks in the $it^{1/2}$ vs $\log t$ plot, as it is the case in the present simulations where phase coexistence is found during intercalation/deintercalation. These authors relate the first peak (p_1 for us) to charge transfer control and p_2 to a mixed charge transfer and diffusion control. Taking this into consideration, we analyze how this change in the global rate control of the process becomes evident in the present simulations. Let us consider insertion at the largest potential step $E_3 \rightarrow E_5$. At the beginning of the transient, Li insertion depends only on the insertion energy barrier (half of the insertion sites are available energetically to insert Li at the interphase), i.e. no other factors are occluding Li insertion (Figure S7a). Under these conditions, lithium insertion is only controlled by charge transfer. When the clog is formed at the interphase

(Figure S7b) Li insertion rate is not only controlled by the insertion energy barrier, but also by the diffusion energy barriers of Li inside graphite. This diffusion generates holes next to the interphase, allowing Li ions to enter the system. Since Li-Li effective interactions in the same layer are attractive, diffusion events from a concentrated Li region (the interphase clog) to a diluted Li zone (an empty lattice area) is slow as compared with the diffusion rate of a single Li ion from a dilute area to a Li ion rich region. Under these conditions, mixed control is expected.

In summary, p_1 can be related to the rate of Li ion (de)insertion at the beginning of the (de)intercalation process, while p_2 is connected with the growth of the phase formed close to the graphite/solution interface.

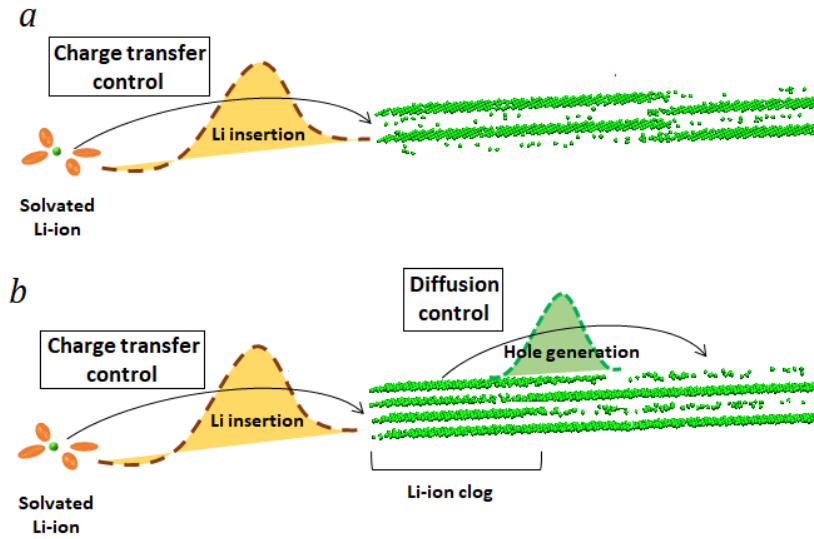


Figure S7. Different global rate control processes at different times for an insertion potential step. The snapshots were taken from a $E_3 \rightarrow E_5$ potential step. Colored curves represent the energy barriers for charge transfer (Li insertion) at the interphase (orange) and diffusion to generate a hole at the Li clog next to the interphase (green). Figure *a* indicates the initial configuration at E_3 , Figure *b* is taken for a time simulation after E_5 is applied, when the Li clog has been formed next to the interphase (minimum in $it^{1/2}$ vs $\log t$ between p_1 and p_2).

S.6. Diffusion supplementary data

This figure illustrates the evolution of the interactions in the system as a function of the lattice occupation x .

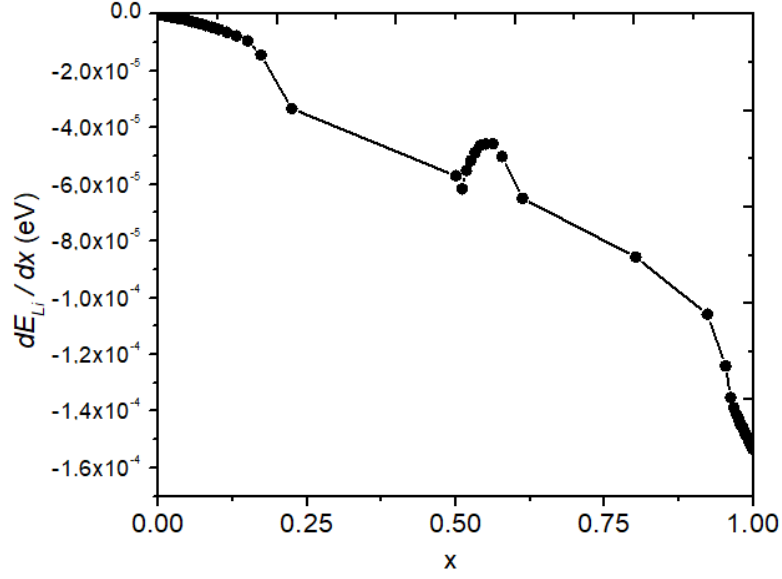


Figure S8: Partial molar energy $\frac{\partial E_{Li}}{\partial x}$ vs x . Where E_{Li} is the energy per Li-ion particle.

S.7. Exchange current density supplementary data

In all cases, the system size used was $24 \times 108 \times 4$ ($L_x = 59.04 \text{ \AA}$, $L_y = 230.04 \text{ \AA}$, $L_z = 13.40 \text{ \AA}$ respectively).

S.7.1. Simulation of the exchange current density

A schematic illustration of Li-ion exchange at the graphite/electrolyte interphase is shown In Figure S9a. A typical time evolution of the different current density contributions, j_{ox} , $|j_{red}|$ and the net current density $|j|$ is presented in Figure S9b, which shows how j_0 was obtained from a deintercalation step. In this case, after reaching a steady state at 120 mV, a potential step was applied to 150 mV. While the main figure shows the separate contributions of j_{ox} and $|j_{red}|$, the inset presents the net current density $j = j_{ox} + j_{red}$ of the system as a function of time. After two seconds, it can be appreciated that j_{ox} and $|j_{red}|$ oscillate around a constant value. We considered that the steady state was reached by analyzing the energy distributions behavior in a Flyvbjerg-Petersen Plot, according to ref. [10].

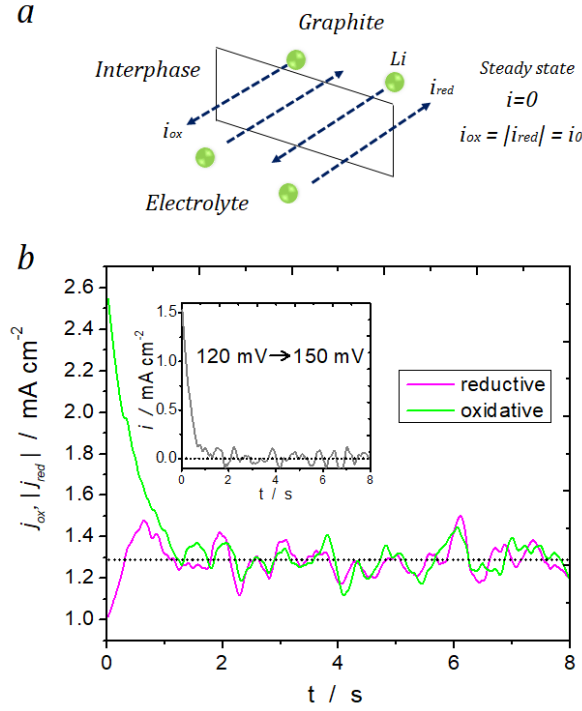


Figure S9: a) Schematic representation of Li-ion exchange at the graphite/electrolyte interphase. b) Contributions of the oxidation current j_{ox} and the absolute value of the reduction current $|j_{red}|$ to the total current density i for a deintercalation potential step between the potential values given in the figure. The inset shows the evolution of the total current density i as a function of time.

S.7.2. Derivation of the exchange current from a Butler-Volmer/Frumkin isotherm

The current flowing for this system can be written as [11]:

$$i = Q \frac{dx}{dt} = Qk_1c_{Li^+} \left\{ (1-x) \exp \left[\frac{\alpha_{BV}F}{RT} (E-E_0) - (1-\alpha_{BV})gx \right] - k_{-1}x \exp \left[-\frac{\alpha_{BV}F}{RT} (E-E_0) + \alpha_{BV}gx \right] \right\} \quad (\text{S21})$$

where Q is the charge corresponding to full occupation of the system ($x=1$), k_1 and k_{-1} are forward and reverse rate constants, F , R and T are the Faraday constant, the ideal gas constant and the temperature, g is an interaction parameter, c_{Li^+} is the Lithium-ion concentration in the solution and α_{BV} the symmetry factor for charge transfer.

Setting $i=0$ in equation (S21) leads to the intercalation isotherm:

$$\frac{x}{1-x} = \frac{k_1}{k_{-1}} c_{Li^+} \exp\left[\frac{F}{RT}(E - E_0)\right] \exp(-gx) \quad (S22)$$

while replacement of (S22) into (S21) leads to the exchange current density:

$$i_0 = Q(k_1)^{1-\alpha_{BV}} (k_{-1})^{\alpha_{BV}} (c_{Li^+})^{1-\alpha_{BV}} (1-x)^{1-\alpha_{BV}} x^{\alpha_{BV}} e^{(2\alpha_{BV}-1)gx} \quad (S23)$$

In the case where $\alpha_{BV} = 0.5$ the previous equation reduces to:

$$i_0 = Qk_1^{0.5} k_{-1}^{0.5} c_{Li^+}^{0.5} (1-x)^{0.5} x^{0.5} \quad (S24)$$

S.7.3. Change of the exchange current density with lattice occupation for a system without repulsive interactions between lithium ions in different graphite planes.

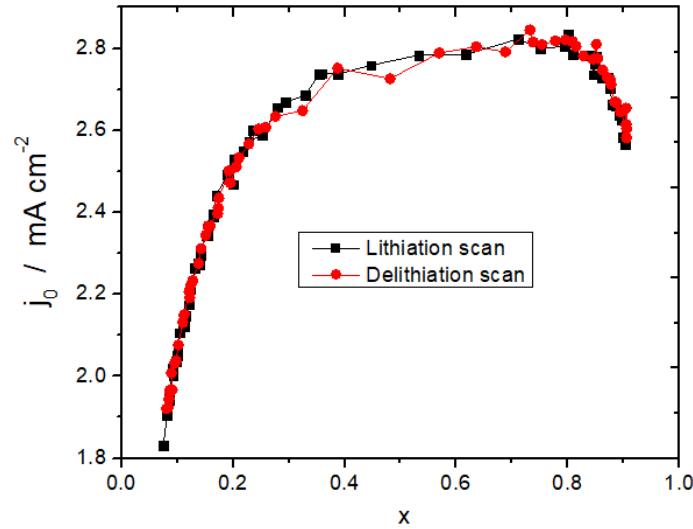


Figure S10: Exchange current density vs lithium composition in graphite kMC simulation at 0.5 mV.s⁻¹ sweep rate, when the repulsive interactions term between lithium ions in different graphite planes are turned-off. Stage II is not formed.

Description of the videos:

KMC-Li-E3-E5.mp4: Video corresponding to the evolution of system configuration over time when simulating a potentiostatic step $E_3 \rightarrow E_5$, where the transition $II \rightarrow I$ occurs. The

video motion starts when the potentiostatic step is applied. Li-ions are represented in green and the graphite substrate is not shown. The simulation box axes are presented at the bottom left corner. The graphite-solution interphase is located on the left side of the box. Each frame corresponds to a time increment $\Delta t \approx 1\text{s}$. The main events occurring are the formation of the stage I Li-ion clog next to the interphase at the beginning and the subsequent growth of stage I towards the inner part of the electrode, until a full stage I occupation is reached.

KMC-Li-current-zero.mp4: This video mimics an experimental situation where no net current flow occurs across the graphite/solution interphase, starting at a time point where a clog has formed at this interphase. Thus, the simulated situation is one where the electrode is left at open circuit potential, after a stage I Li-ion clog has been formed next to the interphase. This clog appeared as a consequence of a potentiostatic step $E_3 \rightarrow E_5$. Li-ions are presented in green and the graphite substrate is not shown. The simulation box axes are presented at the bottom left corner. The graphite-solution interphase is located on the left side of the box. As expected from the experimental conclusions from Inaba et al [12], the electrode potential depends on the stage formed next to the interphase. However, when no current flows, the Li-ion clog disappears and stage II is reestablished at the interphase.

KMC-Li-E3-E4.mp4: Video corresponding to the evolution of system configuration over time for a potentiostatic step $E_3 \rightarrow E_4$. During this potentiostatic step, a transition from stage II to a mixed stage II-stage I is found. The video motion starts when the potentiostatic step is applied. Li-ions are represented in green and the graphite substrate is not shown. The simulation box axes are presented at the bottom left corner. Each frame corresponds to a time increment $\Delta t = 0.66\text{s}$. The first event occurring is the formation of a stage I clog next to the interphase at the beginning of the intercalation process. Then, the Li-ion clog disappears and stage I starts to grow from the inner part of the electrode, until a mixed stage I-stage II with occupation $x \approx 0.8$ is achieved.

KMC-Li-E5-E3.mp4: Video corresponding to a deintercalation process for the potentiostatic step $E_5 \rightarrow E_3$, that is, for the transition stage $II \rightarrow$ stage I . The video starts when the potentiostatic step is applied. Li-ions are represented in green and the graphite substrate is not shown. The simulation box axes are presented at the bottom left corner. The graphite-solution interphase is located on the left side of the box. Each frame corresponds to a time increment $\Delta t = 0.24\text{s}$. When the potentiostatic step is applied, a portion of stage II is immediately formed at the interphase, then stage II grows towards the inner part of the electrode, until reaching an occupation $x \approx 0.5$.

KMC-Li-E4-E3.mp4: Video corresponding to the simulation of a potentiostatic step $E_4 \rightarrow E_3$. The system evolves from a mixed stage I-stage II configuration to a pure stage II arrangement. The video starts when the potentiostatic step is applied. Li-ions are represented in green and the graphite substrate is not shown. The simulation box axes are presented at the bottom left corner. The graphite-solution interphase is located on the left side of the box. Each frame corresponds to a time increment $\Delta t = 0.13\text{s}$. The system motion is similar to that found in the frames of the movie KMC-Li-E5-E3.mp4, but the formation of stage II next to the interphase, at the beginning of the simulation, is slower.

References

- [1] C. Montella, Discussion of the potential step method for the determination of the diffusion coefficients of guest species in host materials, J. Electroanal. Chem. 518 (2002) 61–83. doi:10.1016/S0022-0728(01)00691-X.
- [2] Y. Xin, A. Huang, Q. Hu, H. Shi, M. Wang, Z. Xiao, X. Zheng, Z. Di, P.K. Chu, Barrier Reduction of Lithium Ion Tunneling through Graphene with Hybrid Defects: First-Principles Calculations, Adv. Theory Simulations. 1 (2018) 1700009. doi:10.1002/adts.201700009.
- [3] J. Liu, J. Wang, C. Xu, H. Jiang, C. Li, L. Zhang, J. Lin, Advanced Energy Storage Devices : Basic Principles , Analytical Methods , and Rational Materials Design, Adv. Sci. (2017) 1700322. doi:10.1002/advs.201700322.
- [4] M.D. Levi, D. Aurbach, The mechanism of lithium intercalation in graphite film electrodes in aprotic media. Part 1. High resolution slow scan rate cyclic voltammetric studies and

- modeling, *J. Electroanal. Chem.* 421 (1997) 79–88. doi:10.1016/S0022-0728(96)04832-2.
- [5] T.L. Kulova, A.M. Skundin, Balance between Reversible and Irreversible Processes during Lithium Intercalation in Graphite, *Russ. J. Electrochem.* 42 (2006) 292–299. doi:10.1134/S1023193506030074.
- [6] B. Markovsky, M.D. Levi, D. Aurbach, The basic electroanalytical behavior of practical graphite–lithium intercalation electrodes, *Electrochim. Acta.* 43 (1998) 2287–2304. doi:10.1016/S0013-4686(97)10172-4.
- [7] M.D. Levi, D. Aurbach, Simultaneous Measurements and Modeling of the Electrochemical Impedance and the Cyclic Voltammetric Characteristics of Graphite Electrodes Doped with Lithium, *J. Phys. Chem. B.* 101 (1997) 4630–4640. doi:10.1021/jp9701909.
- [8] M.D. Levi, E. Markevich, D. Aurbach, The Effect of Slow Interfacial Kinetics on the Chronoamperometric Response of Composite Lithiated Graphite Electrodes and on the Calculation of the Chemical Diffusion Coefficient of Li Ions in Graphite, *J. Phys. Chem. B.* 109 (2005) 7420–7427. doi:https://doi.org/10.1021/jp0441902.
- [9] M.D. Levi, E. Markevich, D. Aurbach, Comparison between Cottrell diffusion and moving boundary models for determination of the chemical diffusion coefficients in ion-insertion electrodes, *Electrochim. Acta.* 51 (2005) 98–110. doi:10.1016/j.electacta.2005.04.007.
- [10] S.A. Paz, E.P.M. Leiva, Time recovery for a complex process using accelerated dynamics, *J. Chem. Theory Comput.* 11 (2015) 1725–1734. doi:10.1021/ct5009729.
- [11] H. Angerstein-Kozłowska, J. Klinger, B.E. Conway, Computer Simulation of the Kinetic Behaviour of the Surface Reactions Driven by a Linear potential Sweep. Part 1. Model 1-Electron Reaction With a Single Adsorbed Species, *J. Electroanal. Chem.* 75 (1977) 45–60. doi:https://doi.org/10.1016/S0022-0728(77)80071-5.
- [12] M. Inaba, H. Yoshida, Z. Ogumi, T. Abe, Y. Mitzutani, M. Asano, In Situ Raman Study on Electrochemical Li Intercalation into Graphite, *J. Electrochem. Soc.* 142 (1995) 20. doi:10.1149/1.2043869.